Electronic Supplementary Information

Experiment Section

Materials: Sodium molybdate dihydrate ($Na_2MoO_4 \cdot 2H_2O$), titanium (IV) isopropoxide ($C_{12}H_{28}O_4Ti$) and potassium hydroxide (KOH) were purchased from Aladdin Industrial Co., isopropyl alcohol (C_3H_8O) was obtained from Zhiyuan Chemical Reagent Co.. Nafion solution (5 wt%) was purchased from Sigma-Aldrich. All chemicals were used as received without further purification.

Synthesis of Mo-TiO_2 and TiO_2: $Na_2MoO_4 \cdot 2H_2O$ (0.447 g) was dissolved in 20 mL deionized water and vigorously stirred for 10 min. Then 6 mL titanium (IV) isopropoxide was added to the solution drop by drop and continued to stir for 1 h at 80°C. The resulting solution was transferred to a 40 mL Teflon autoclave, and heated at 180°C for 12 h in an oven. The product (Mo-TiO_2-2) was collected by centrifugation and washed with deionized water and ethanol, and then dried at 60°C in a vacuum oven. Moreover, different proportions of Mo doping were synthesized by the same method (0.212 g $Na_2MoO_4 \cdot 2H_2O$ named Mo-TiO_2-1, 1.007 g $Na_2MoO_4 \cdot 2H_2O$ named Mo-TiO_2-3). For comparison, pure TiO_2 was synthesized by the similar method without $Na_2MoO_4 \cdot 2H_2O$.

Characterization: The morphologies and microstructures were investigated by transmission electron microscopy (TEM, FEI TF20). X-ray diffraction (XRD) patterns were obtained from an XRD-6100 (XRD, Shimadzu XRD-6100) with Cu Kα source radiation at a scanning rate of 5° min^{-1} from 10° to 80°. The surface properties of the samples were studied by X-ray photoelectron spectroscopy (XPS, ESCALABMK II). The absorbance data of spectrophotometer were acquired on Ultraviolet-visible (UV-Vis) spectrophotometer (Shimadzu UV-2700). Electron paramagnetic resonance (EPR) spectra were obtained on a Bruker 500 spectrometer at 77 K.

Electrochemical measurements: 10 mg of Mo-TiO_2 or TiO_2 powder was mixed with

20 uL 5wt% Nafion solution and ultrasonically dispersed in 0.98 mL isopropyl alcohol solution. Then, 10 μL the catalyst ink was loaded onto a pre-polished glassy carbon electrode (D = 5.6 mm) of a rotation ring disk electrode (RRDE) to achieve a catalyst loading ≈ 0.4 mg cm^{-2}. All electrochemical were carried on CHI 760E (CHI Instruments Inc.). The RRDE loaded with electrocatalyst, graphite rod and Hg/HgO (saturation KOH) were used as the working electrode, counter electrode and reference electrode, respectively. The electrolyte was 0.1 M KOH. The linear sweep voltammetry (LSV) was tested by RRDE scans from 0 to 1.0 V versus reversible hydrogen electrode (V_{RHE}) in O_2-saturated 0.1 M KOH at a scan rate of 10 mV s^{-1} and a rotation speed of 1600 rpm. During the LSV, the Pt ring potential was held at 1.2 V_{RHE}. The electrochemical impedance spectroscopy (EIS) was conducted at 0.65 V_{RHE} from 1,000,000 to 0.1 Hz. The H_2O_2 selectivity (H_2O_2 (%)) and electron transfer number (n) were calculated from the RRDE measurement according to following equation:

$$H_2O_2\ (\%) = 200\times(I_{Ring}/N)/(I_{Disk}+I_{Ring}/N) \quad (1)$$

$$n = 4I_{Disk}/(I_{Disk}+I_{Ring}/N) \quad (2)$$

Where I_{Disk} is the measured current of disk electrode, I_{Ring} is the measured current of Pt ring electrode, N is the collection efficiency of Pt ring (0.37).

Electrogeneration of H_2O_2: The electrogeneration of H_2O_2 were conducted in H-type cell with nafion membrane as separator. Cathode was prepared by depositing catalyst ink (10 μL, 10 mg mL^{-1}) on a carbon paper (CP) (1×1 cm). Hg/HgO (saturation KOH) and graphite rod were used as the reference electrode and counter electrode, respectively. The electrolyte was O_2-saturated 0.1 M KOH (30 mL). H_2O_2 yield was measured by using the indicator of $Ce(SO_4)_2$ ($2Ce^{4+} + H_2O_2 \rightarrow 2Ce^{3+} + 2H^+ + O_2$). Samples (200 μL test electrolyte) were collected at a certain time (1 h) and mixed with the Ce^{4+} solution (0.1 mM, 5.8 mL). The mixed solution was detected with UV-vis spectrophotometer. A typical concentration-absorbance curve was calibrated by linear fitting the absorbance values at wavelength length of 318 nm for various standard concentrations of 0.02, 0.04, 0.06, 0.08, 0.1 mM of Ce^{4+}. The fitting curve (y

= 4.3365 x − 0.00881, R^2= 0.999) shows good linear relation of absorbance value with Ce^{4+} concentration (Fig. S13). The yield of H_2O_2 was finally determined based on the reduced Ce^{4+} concentration.

The density functional theory (DFT) calculation details: The first principle calculations were performed to reveal the mechanism of ORR on the surface of Mo-TiO_2 by using the Vienna ab initio simulation package (VASP).[1,2] The generalized gradient approximation method of Perdew-Burke-Ernzerhof (PBE) functional was used to describe the exchange-related interaction between electrons.[3] U (Ti_{3d}) value of 3.5 eV and U (Mo_{3d}) value of 3.0 eV were applied to the Ti_{3d} and Mo_{3d} states.[4,5] The van der Waals (vdW) correction with the Grimme approach (DFT-D2) was included in the interaction between single molecule/atoms and substrates.[6] The energy cutoff for the plane wave-basis expansion was set to 500 eV. The convergence criteria for the total energy and the Hellmann-Feynman force were 10^{-5} eV and 0.02 eVÅ^{-1}, respectively. The TiO_2 (101) surface was modeled using a 2 × 2 slab with four trilayers (O-Ti-O) that the bottom trilayer is fixed, separated by 15 Å of vacuum. The Brillouin zone was sampled with 3 × 3 × 1 Gamma-center k-point mesh.

The formation energies of oxygen vacancy on Mo-TiO_2 (101) are defined as an equation:

$$E_f = E(\text{Mo-TiO}_m) + E(O_2)/2 - E(\text{Mo-TiO}_{m-1}) \quad (3)$$

Where E_f is the formation energy, $E(\text{Mo-TiO}_m)$ and $E(\text{Mo-TiO}_{m-1})$ is the total energies without and with oxygen vacancy, $E(O_2)$ is the total energy of single oxygen gas, m is the number of O atoms in surface supercell.

The computational hydrogen electrode model has been adopted for calculations of the Gibbs free-energy change for the relevant elemental steps, which can be obtained by $\Delta G = \Delta E + \Delta E_{ZPE} - T\Delta S$, where ΔE is the total energy, ΔE_{ZPE} is the zero point energy and S is the entropy at 298.15 K. The theoretical overpotential (η) of $2e^-$ ORR was deduced using the equation of $\eta = |\Delta G_{*OOH}/e - 4.22\ V|$. The solvation effect was not considered in determining the value of ΔG_{*OOH}, which governs a

reasonable comparison.

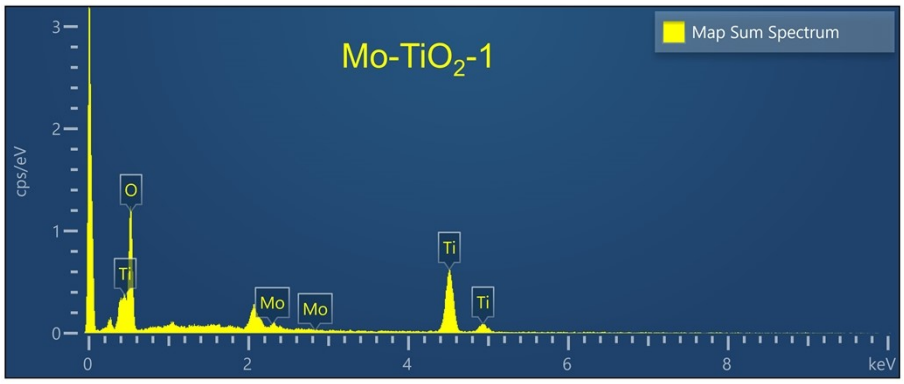

Element	Line Type	Apparent Concentration	k Ratio	Wt%	Atomic %
O	K series	66.54	0.22390	37.33	64.71
Ti	K series	117.38	1.17377	59.24	34.30
Mo	L series	6.06	0.06058	3.43	0.99
Total:				100.00	100.00

Fig. S1. EDX spectrum of Mo-TiO_2-1.

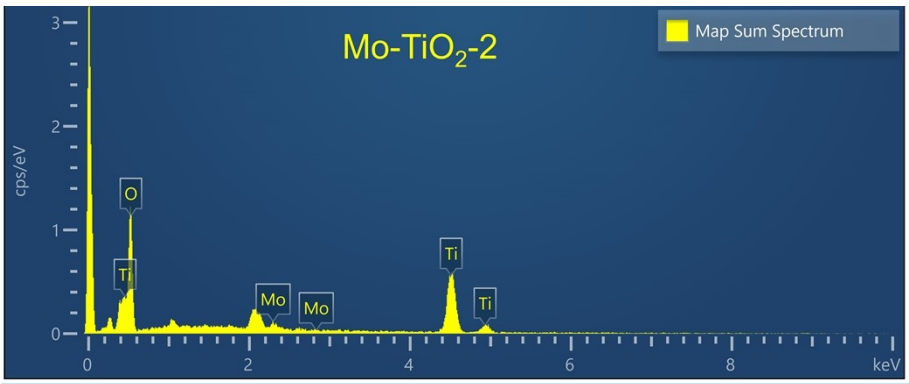

Element	Line Type	Apparent Concentration	k Ratio	Wt%	Atomic %
O	K series	64.33	0.21648	37.38	64.96
Ti	K series	110.42	1.10415	58.12	33.73
Mo	L series	7.61	0.07614	4.50	1.30
Total:				100.00	100.00

Fig. S2. EDX spectrum of Mo-TiO_2-2.

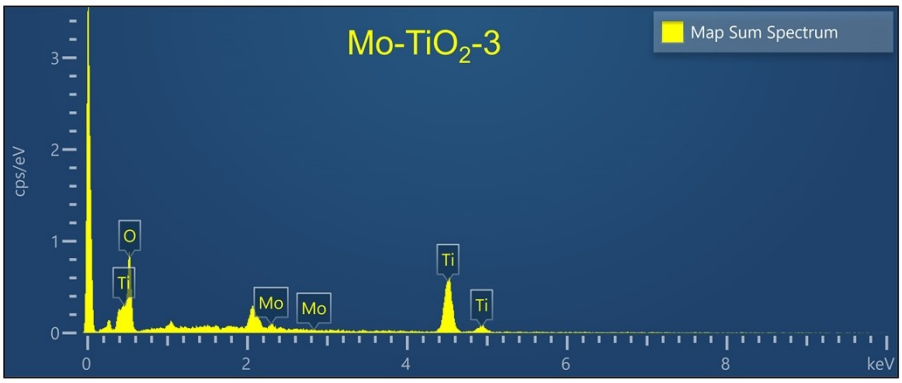

Element	Line Type	Apparent Concentration	k Ratio	Wt%	Atomic %
O	K series	46.52	0.15654	31.04	58.25
Ti	K series	117.19	1.17192	64.27	40.28
Mo	L series	7.60	0.07605	4.69	1.47
Total:				100.00	100.00

Fig. S3. EDX spectrum of Mo-TiO_2-3.

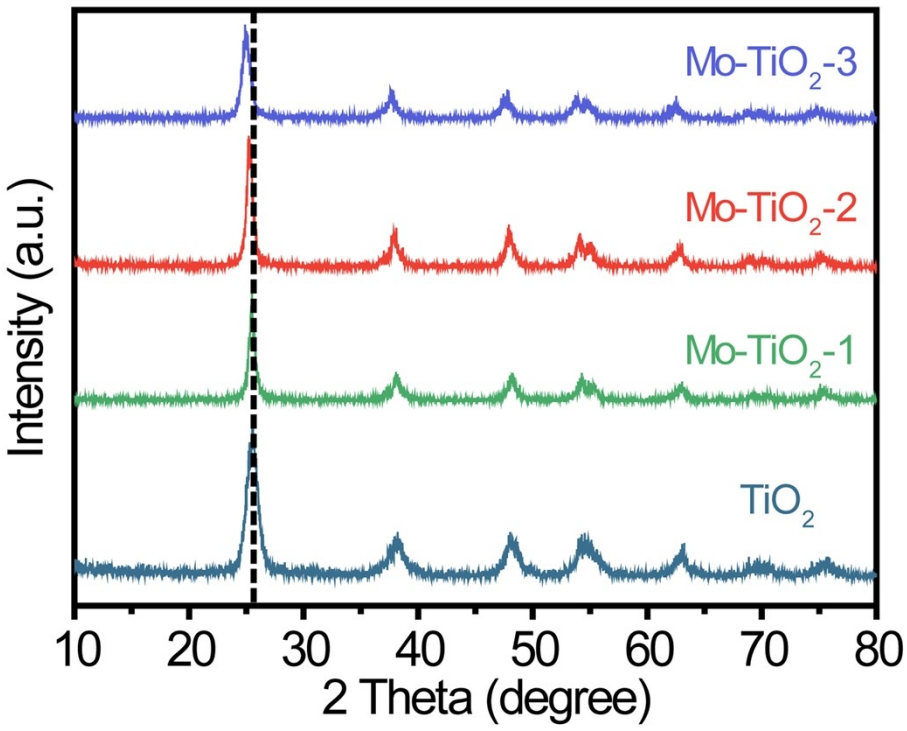

Fig. S4. XRD patterns of TiO_2, Mo-TiO_2-1, Mo-TiO_2-2 and Mo-TiO_2-3.

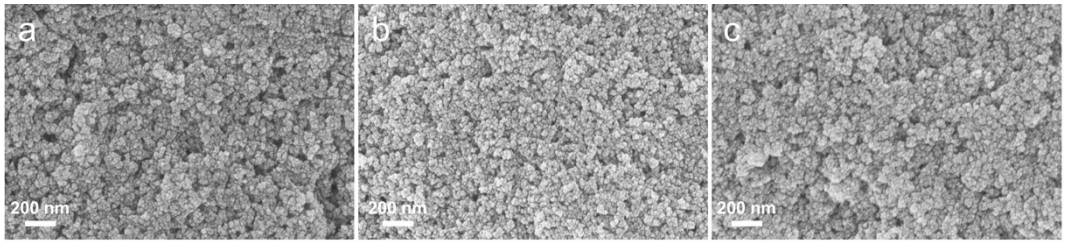

Fig. S5. SEM images of (a) Mo-TiO_2-1, (b) Mo-TiO_2-2 and (c) Mo-TiO_2-3.

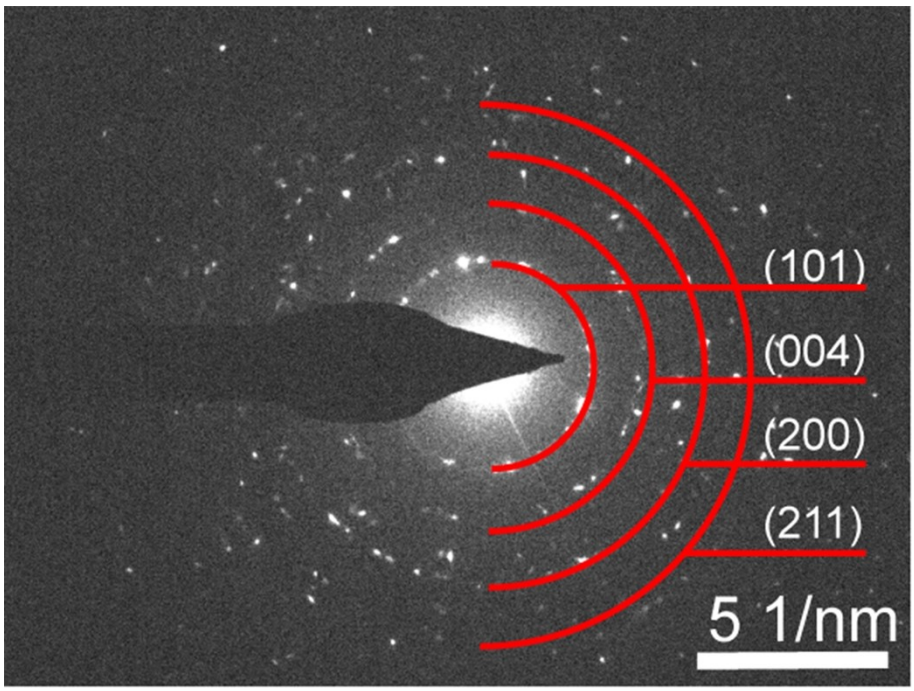

Fig. S6. SAED pattern of Mo-TiO_2-2.

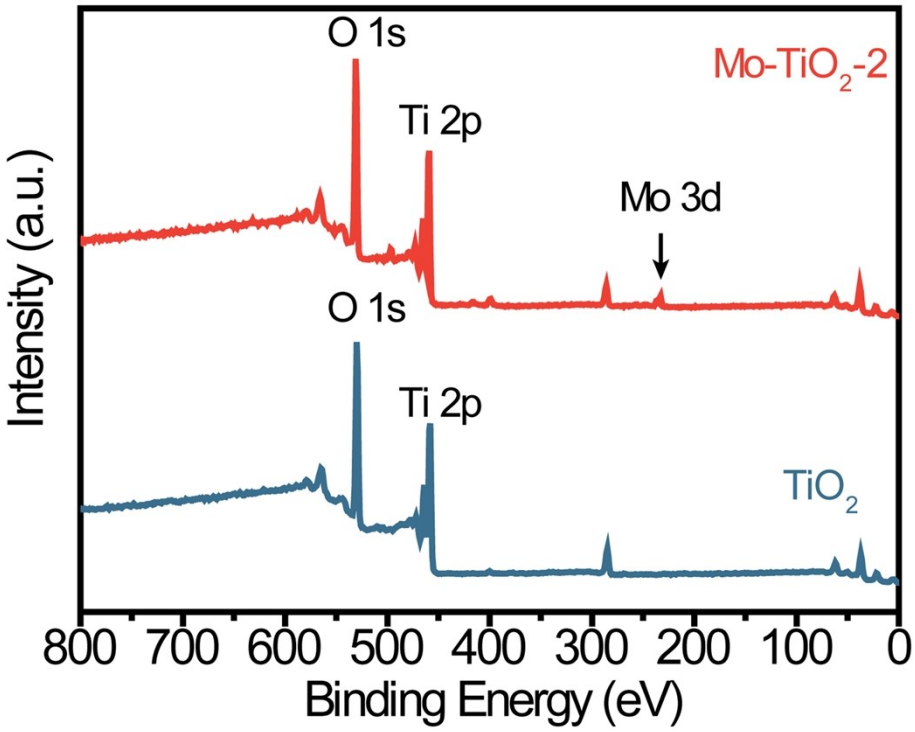

Fig. S7. Survey XPS spectra of TiO_2 and Mo-TiO_2-2.

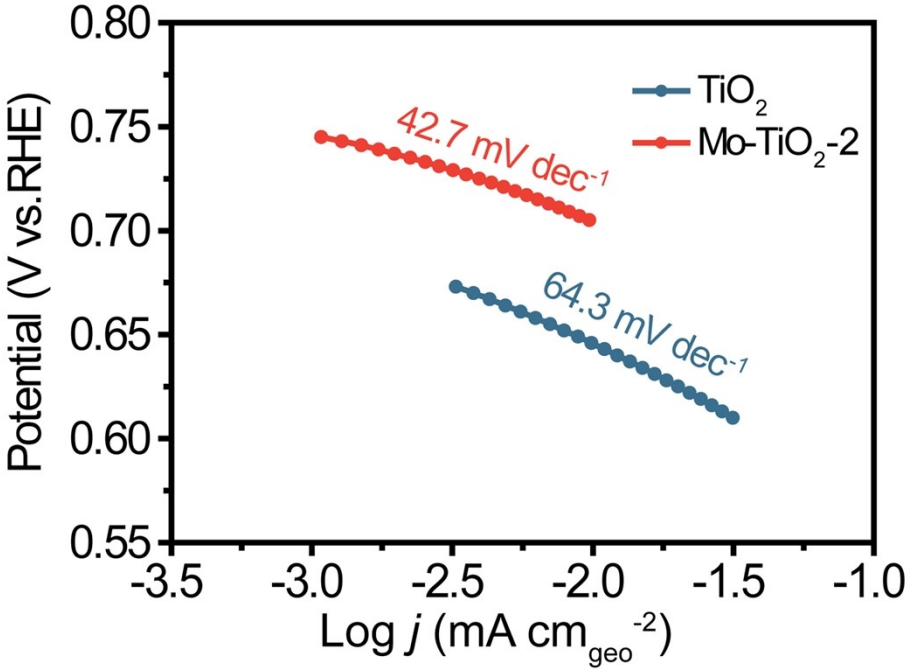

Fig. S8. Tafel plots of TiO_2 and Mo-TiO_2-2 in 0.1 M KOH.

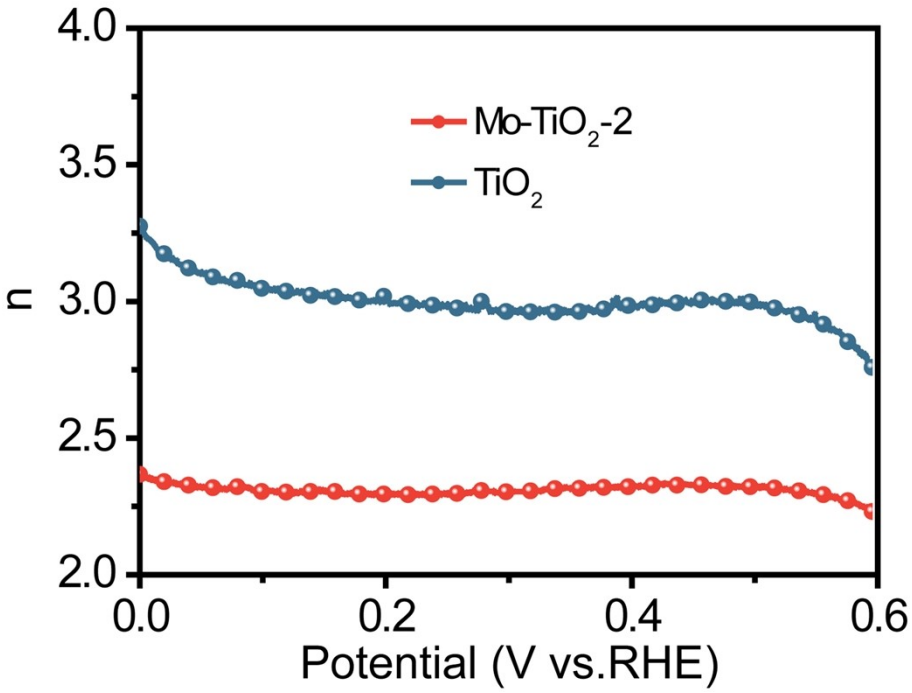

Fig. S9. Electron transfer numbers (n) for TiO_2 and Mo-TiO_2-2.

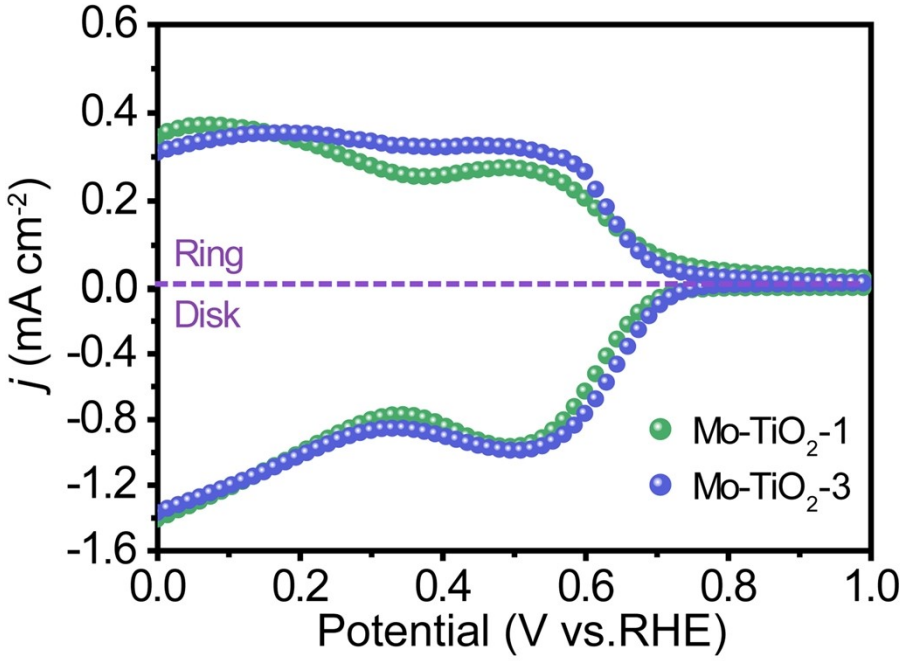

Fig. S10. LSV curves of Mo-TiO_2-1 and Mo-TiO_2-3.

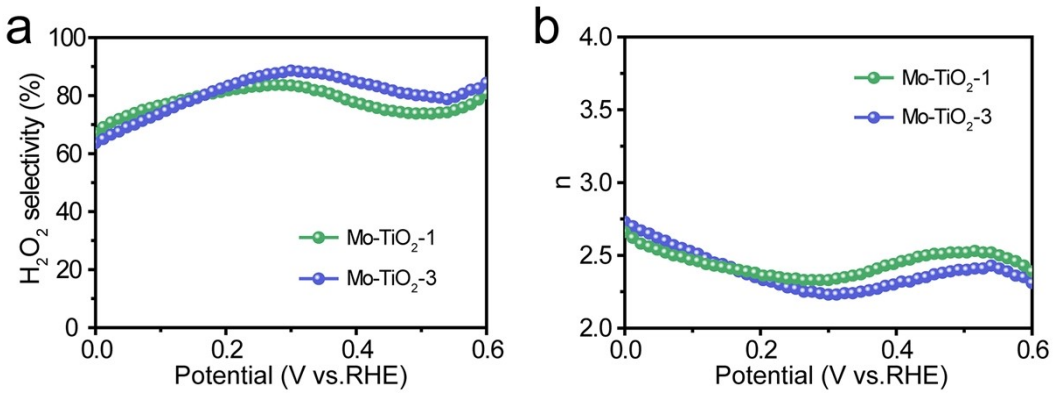

Fig. S11. (a) H_2O_2 selectivity and (b) electron transfer numbers (n) of Mo-TiO_2-1 and Mo-TiO_2-3.

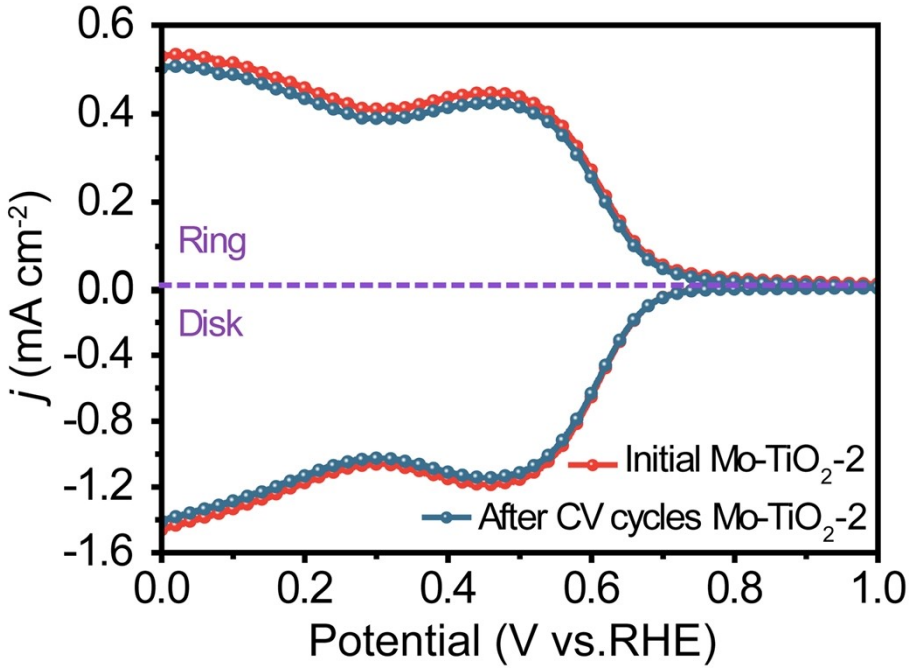

Fig. S12. LSV curves of Mo-TiO_2-2 for 3000 CV cycles before and after.

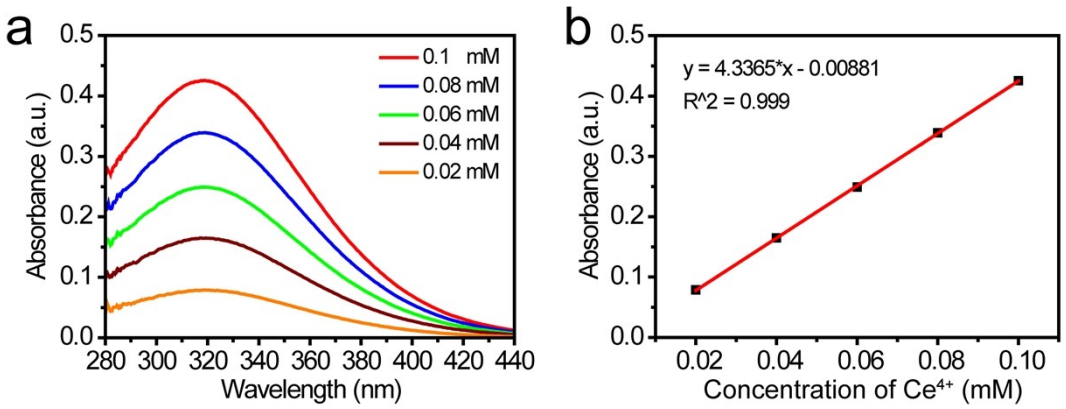

Fig. S13. (a) UV-Vis spectra of Ce^{4+} solution with various concentrations and (b) corresponding standard curve.

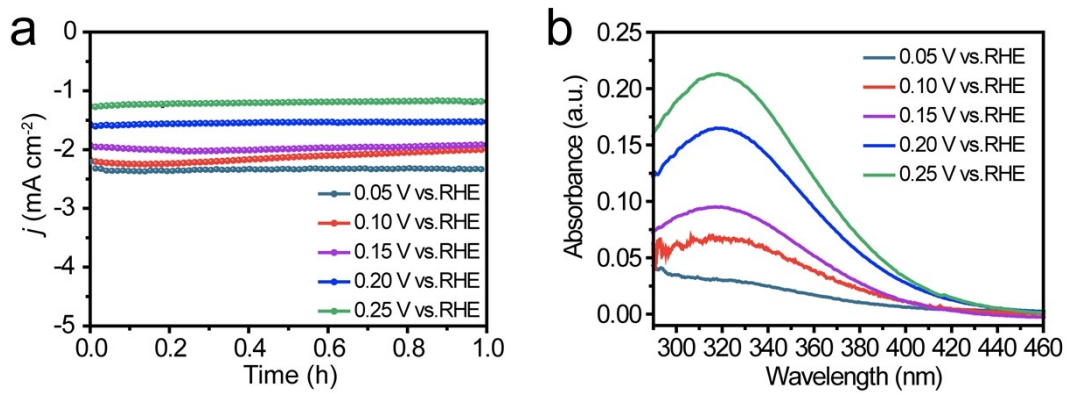

Fig. S14. (a) Time-dependent current density curves of Mo-TiO_2-2 under various potentials for 1 h. (b) UV-Vis spectra of electrolyte with various potential.

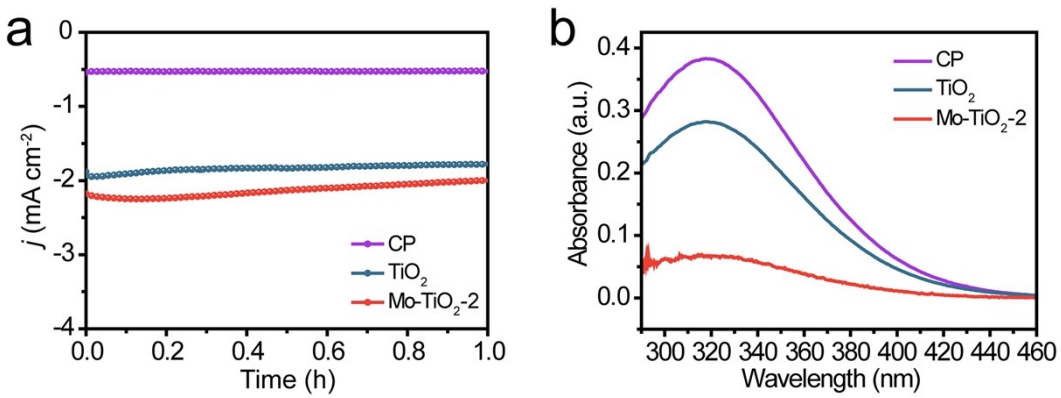

Fig. S15. (a) Time-dependent current density curves of pure CP, TiO_2 and Mo-TiO_2-2 for 1 h. (b) UV-Vis spectra of electrolyte for pure CP, TiO_2 and Mo-TiO_2-2.

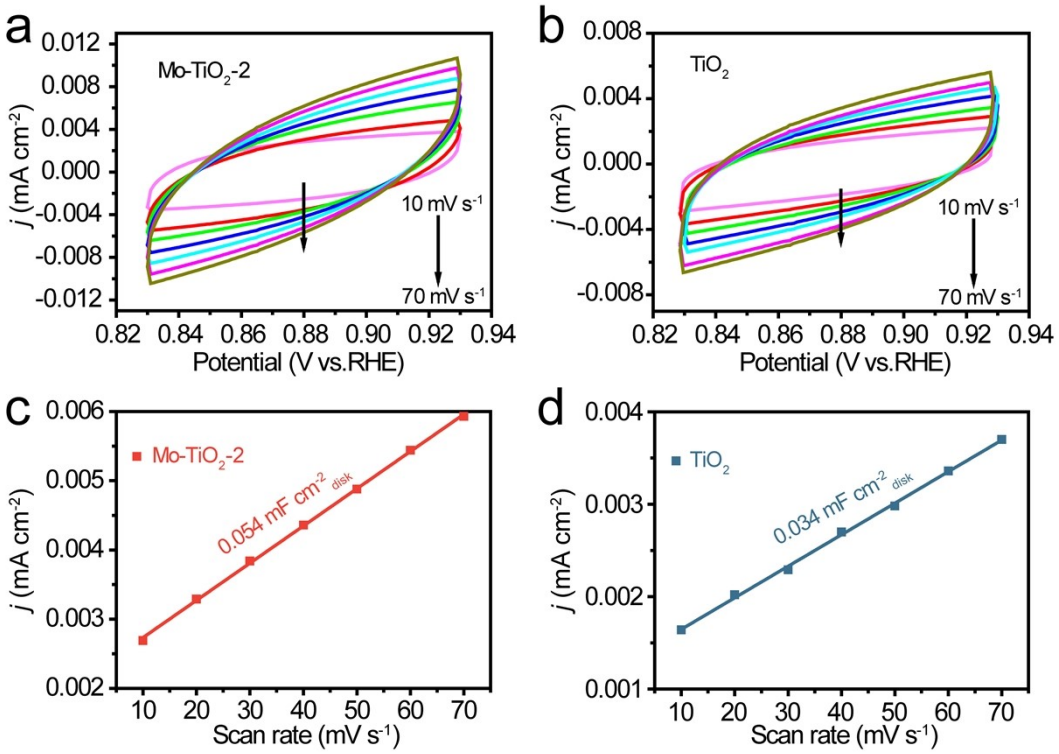

Fig. S16. CV curves for (a) Mo-TiO_2-2 and (b) TiO_2 in the double layer region at scan rates of 10, 20, 30, 40, 50, 60 and 70 mV s^{-1} in 0.1 M KOH. Capacitive currents as a function of scan rate for (c) Mo-TiO_2-2 and (d) TiO_2 at 0.88 V_{RHE}.

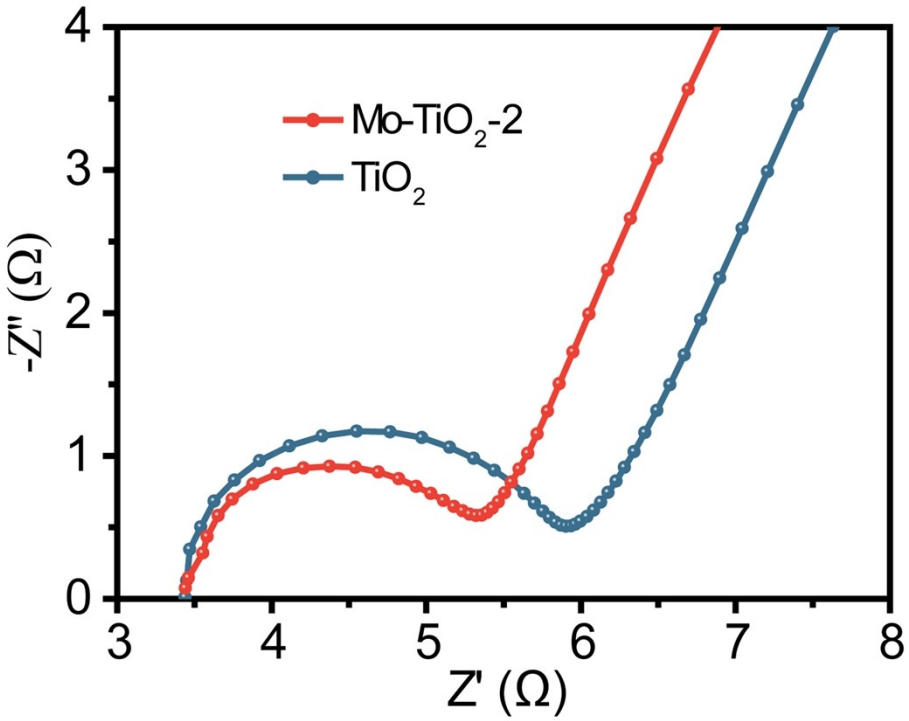

Fig. S17. Nyquist plots of TiO_2 and Mo- TiO_2-2.

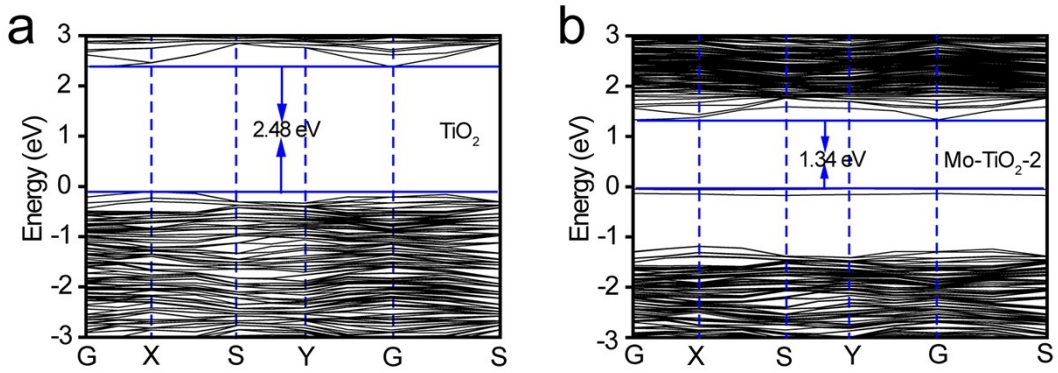

Fig. S18. Band structures of (a) TiO_2 and (b) Mo-TiO_2-2.

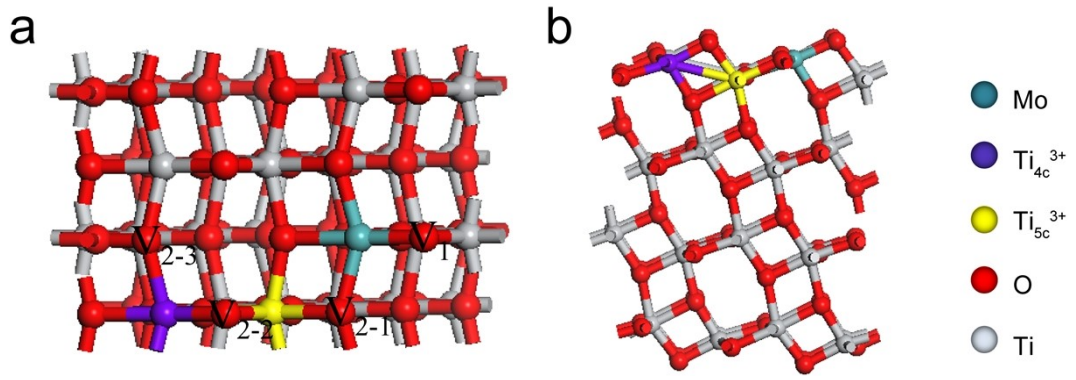

Fig. S19. (a) Front view and (b) vertical view of possible oxygen vacancy distributions of Mo-TiO_2 (101) surface.

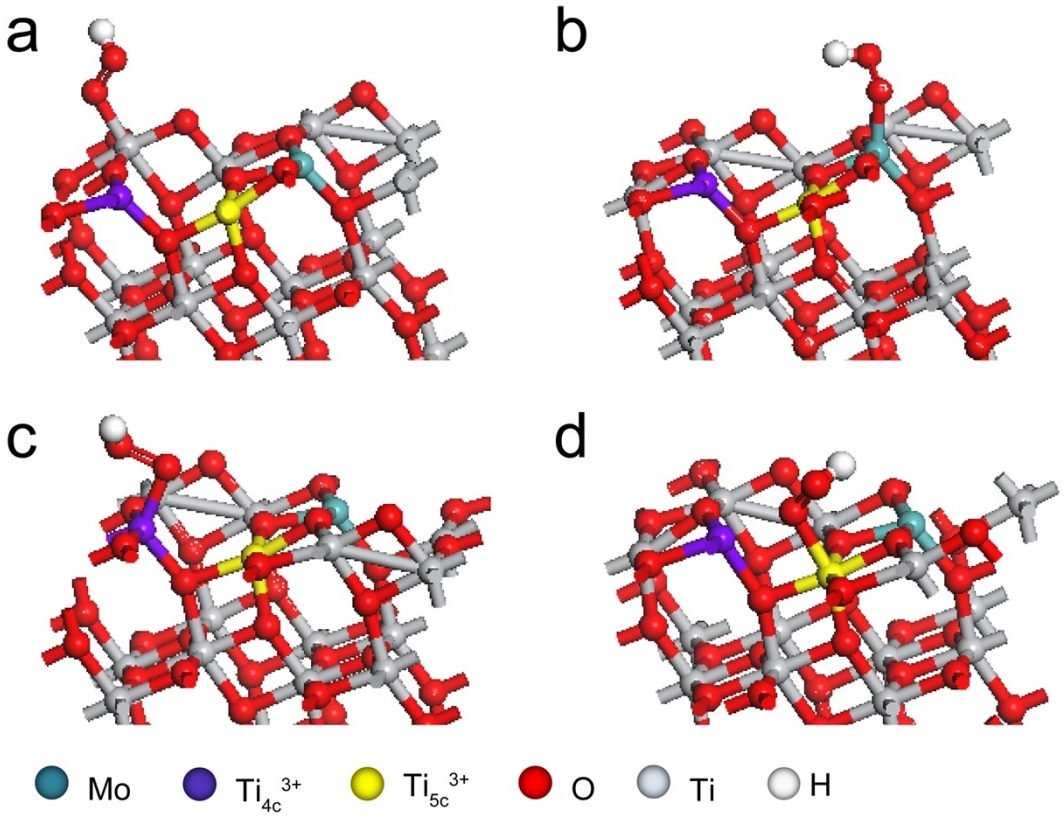

Fig. S20. Atom configurations of the *OOH absorption at (a) Ti^{4+}, (b) Mo, (c) Ti_{4c}^{3+} and (d) Ti_{5c}^{3+} sites.

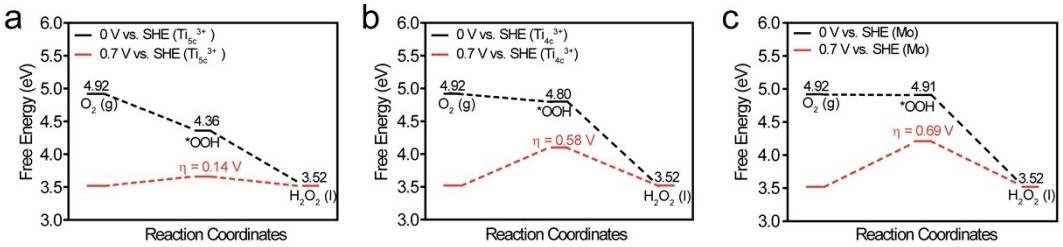

Fig. S21. Free energy diagrams with the theoretical overpotentials (η) of the $2e^-$ ORR at the zero potential (black line) and the equilibrium potential (red line) for (a) Ti_{5c}^{3+}, (b) Ti_{4c}^{3+} and (c) Mo sites.

Table S1. Comparison of performance for Mo-TiO_2 with other reported $2e^-$ ORR electrocatalysts.

Catalyst	Electrolyte	Selectivity@potential (% @ V_{RHE})	Productivity	Ref.
Mo-TiO_2-2	0.1 M KOH	86@0.2	395.3 mmol g_{cat}^{-1} h^{-1}	This work
TiO_2		52@0.3	134.1 mmol g_{cat}^{-1} h^{-1}	
TiO_2-Au/C 3%	1.0 M NaOH	75	/	7
Au/TiO_2	0.1 M KOH	90@0.1	/	8
CuO_x/G-30	1.0 M KOH	80@0.5	/	9
Fe_3O_4/Printex	1.0 M KOH	68@0.4	/	10
Fe_3O_4/graphene		62@0.4	/	
Nb_2O_5-rGO	0.1 M NaOH	74.9@0.4	/	11
4% CeO_2/C-PPM-P	1.0 M NaOH	88	/	12
$Sr_{0.7}Na_{0.3}Si_{0.95}Cu_{0.05}O_3$	0.1 M KOH	78@0.4	/	13
O-CNTs	0.1 M KOH	88@0.4	111.7 mmol g_{cat}^{-1} h^{-1}	14
HPCS-S	0.1 M KOH	71@0.4	0.184 mol g_{cat}^{-1} h^{-1}	15
Col-NG(O)	0.1 M KOH	80@0.4	~418 mmol g_{cat}^{-1} h^{-1}	16
Ni MOF NSs-6	0.1 M KOH	95@0.5	80 mmol g_{cat}^{-1} h^{-1}	17
rGO/PEI	0.1 M KOH	90.7@0.74	0.106 mol g_{cat}^{-1} h^{-1}	18
OCB-120	0.1 M KOH	63.5@0.36	/	19
G/CDs	0.1 M KOH	71-82@0.35-0.72	/	20
oxo-G/$NH_3 \cdot H_2O$	0.1 M KOH	>82	224.8 mmol g_{cat}^{-1} h^{-1}	21
G-COF-950	0.1 M KOH	75	1286.9 mmol g^{-1} h^{-1}	22
5-Ni_3(HITP)$_2$	0.1 M KOH	80	/	23
Pt-Ag alloy	0.05 M Na_2SO_4 (pH = 3)	70-90	236.25 mol kg^{-1} h^{-1}	24
$Pd^{\delta+}$-OCNT	0.1 M $HClO_4$	95-98@0.3-0.7	1701 mol kg^{-1} h^{-1}	25
Pt–Hg	0.1 M $HClO_4$	96@0.2-0.4	/	26
a-TiO_{2-x}/TiC	0.1 M KOH	94@0.5	7.19 mol g_{cat}^{-1} h^{-1}	27

References

1 G. Kresse and J. Furthmüller, *Comp. Mater. Sci.*, 1996, **6**, 15−50.

2 G. Kresse and J. Furthmüller, *Phys. Rev. B*, 1996, **54**, 11169.

3 J. P. Perdew, K. Burke and M. Ernzerhof, *Phys. Rev. Lett.*, 1996, **77**, 3865−3868.

4 A. Tilocca and A. Selloni, *J. Phys. Chem. C*, 2012, **116**, 9114−9121.

5 M. García-Mota, A. Vojvodic, F. Abild-Pedersen and J. K. Nørskov, *J. Phys. Chem. C*, 2013, **117**, 460−465.

6 S. Grimme, J. Antony, S. Ehrlich and H. Krieg, *J. Chem. Phys.*, 2010, **132**, 154104.

7 F. V. E. Reis, V. S. Antonin, P. Hammer, M. C. Santos and P. H. C. Camargo, *J. Catal.*, 2015, **326**, 100–106.

8 Z. Sun, L. Sheng, H. Gong, L. Song, X. Jiang, S. Wang, X. Meng, T. Wang and J. He, *Chem. Asian J.*, 2020, **15**, 4280–4285.

9 H. Xiao, B. Li, M. Zhao, Y. Li, T. Hu, J. Jia and H. Wu, *Chem. Commun.*, 2021, **57**, 4118–4121.

10 W. R. P. Barros, Q. Wei, G. Zhang, S. Sun, M. R. V. Lanza and A. C. Tavares, *Electrochim. Acta*, 2015, **162**, 263–270.

11 J. F. Carneiro, M. J. Paulo, M. Siaj, A. C. Tavares and M. R. V. Lanza, *J. Catal.*, 2015, **332**, 51–61.

12 M. H. M. T. Assumpcão, A. Moraes, R. F. B. D. Souza, M. L. Calegaro, M. R. V. Lanza, E. R. Leite and M. A. L. Cordeiro, *Electrochim. Acta*, 2013, **111**, 339–343.

13 S. Thundiyil, S. Kurungot and R. N. Devi, *ACS Appl. Mater. Interfaces*, 2021, **13**, 382–390.

14 Z. Lu, G. Chen, S. Siahrostami, Z. Chen, K. Liu, J. Xie, L. Liao, T. Wu, D. Lin, Y. Liu, T. F. Jaramillo, J. K. Nørskov and Y. Cui, *Nat. Catal.*, 2018, **1**, 156–162.

15 G. Chen, J. Liu, Q. Li, P. Guan, X. Yu, L. Xing, J. Zhang and R. Che, *Nano Res.*, 2019, **12**, 2614–2622.

16 E. Jung, H. Shin, B. H. Lee, V. Efremov, S. Lee, H. S. Lee, J. Kim, W. H. Antink,

S. Park, K. S. Lee, S. P. Cho, J. S. Yoo, Y. E. Sung and T. Hyeon, *Nat. Mater.*, 2020, **19**, 436–442.

17 M. Wang, X. Dong, Z. Meng, Z. Hu, Y. Lin, C. Peng, H. Wang, C. Pao, S. Ding, Y. Li, Q. Shao and X. Huang, *Angew. Chem. Int. Ed.*, 2021, **60**, 11190–11195.

18 X. Xiao, T. Wang, J. Bai, F. Li, T. Ma and Y. Chen, *ACS Appl. Mater. Interfaces*, 2018, **10**, 42534–42541.

19 X. Lu, D. Wang, K.-H. Wu, X. Guo and W. Qi, *J. Colloid Interface Sci.*, 2020, **573**, 376–383.

20 Y. Dong, J. Su, S. Zhou, M. Wang, S. Huang, C.-H. Lu, H. Yang and F. Fu, *Chem. Commun.*, 2020, **56**, 7609−7612.

21 L. Han, Y. Sun, S. Li, C. Cheng, C. E. Halbig, P. Feicht, J. L. Hübner, P. Strasser and S. Eigler, *ACS Catal.*, 2019, **9**, 1283−1288.

22 J. Zhang, G. Zhang, S. Jin, Y. Zhou, Q. Ji, H. Lan, H. Liu and J. Qu, *Carbon*, 2020, **163**, 154–161.

23 M. Liu, H. Zhang, Y. Li, H. Su, W. Zhou, X. Zhao, W. Cheng and Q. Liu, *Chem. Commun.*, 2020, **56**, 5299–5302.

24 Y.-J. Ko, K. Choi, B. Yang, W. H. Lee, J.-Y. Kim, J.-W. Choi, K. H. Chae, J. H. Lee, Y. J. Hwang, B. K. Min, H.-S. Oh and W.-S. Lee, *J. Mater. Chem. A*, 2020, **8**, 9859–9870.

25 Q. Chang, P. Zhang, A. H. B. Mostaghimi, X. Zhao, S. R. Denny, J. H. Lee, H. Gao, Y. Zhang, H. L. Xin, S. Siahrostami, J. G. Chen and Z. Chen, *Nat. Commun.*, 2020, **11**, 2178.

26 S. Siahrostami, A. Verdaguer-Casadevall, M. Karamad, D. Deiana, P. Malacrida, B. Wickman, M. Escudero-Escribano, E. A. Paoli, R. Frydendal, T. W. Hansen, I. Chorkendorff, I. E. L. Stephens and J. Rossmeisl, *Nat. Mater.*, 2013, **12**, 1137−1143.

27 Z. Xu, J. Liang, Y. Wang, K. Dong, X. Shi, Q. Liu, Y. Luo, T. Li, Y. Jia, A. M. Asiri, Z. Feng, Y. Wang, D. Ma and X. Sun, *ACS Appl. Mater. Interfaces*, 2021, **13**, 33182−33187.